Impact of frequency-dependent anisotropy on azimuthal P-wave reflections

Impact of frequency-dependent anisotropy on azimuthal P-wave reflections

Zhaoyu Jin[1, *], Mark Chapman[1], Giorgos Papageorgiou[1, 2] and Xiaoyang Wu[3]

1. School of GeoSciences, The University of Edinburgh, Grant Institute, James Hutton Road, Edinburgh, EH9 3FE, UK.

2. Department of Geoscience, NTNU, S.P. Andersensvei 15A, 7491 Trondheim, Norway.

3. Edinburgh Anisotropy Project, British Geological Survey, The Lyell Centre, Research Avenue South, Edinburgh, EH14 4AP, UK.

* E-mail: Zhaoyu.Jin@ed.ac.uk

Abstract

Seismic anisotropy has widely been used for the characterization of fractures in a reservoir. Recent work has demonstrated the effect of seismic dispersion on producing a frequency-dependent reflection coefficient, which can be important in fracture characterization since large fractures often lead to frequency-dependent anisotropy. In this paper, we examine the impact of anisotropic dispersion on P-wave reflections based on an HTI sand model overlaid by VTI shale. Although VTI in the overburden does not lead to azimuthal anisotropy, its effect on angle dependence could significantly affect the azimuthal AVO responses at far offsets. We show a modest effect on the amplitude and large effect on the phase, the latter of which could even be mistaken for azimuthal velocity variations. We present a Bayesian inversion based on a forward modelling technique aimed at recovering water saturation, fracture density and fracture length of a HTI sand. Our results show potential of using seismic dispersion in azimuthal AVO analysis to discriminate large-scale fractures from micro-scale cracks.

Keywords

Frequency-dependent anisotropy; Fractures; Azimuthal AVO; Transverse isotropy; Partial saturation

Introduction

The detection of fractures in a reservoir is of great interest because fracturing can significantly affect fluid flow during hydrocarbon production. Studies on the variation of P-wave reflectivity with azimuth and offset have gained much attention since it can be analysed to determine the orientation and density of fractures (e.g., Lynn et al. 1995, Rüger 1998, Hall and Kendall 2003). However, the estimation of fracture sizes from azimuthal P-wave reflection remains a challenge since conventional seismic anisotropy is assumed insensitive to the fracture length (Hudson 1981, Liu et al. 2000).

It is known that the presence of fractures in a reservoir often leads to frequency-dependent anisotropy (FDA), which has been observed by Marson-Pidgeon and Savage (1997), Chesnokov et al. (2001) and Al-Harrasi et al. (2011). A large amount of literature also exits on the development of rock physics theories that describe such fracture-induced dispersion (e.g., Chapman 2003, Gurevich 2003, Brajanovski et al. 2005, Liu et al. 2006, Chapman 2009, Jakobsen and Chapman 2009, Guo et al. 2016, Collet and Gurevich 2016). During the past decade, attention has increasingly been paid to the effect of seismic dispersion on reservoir characterization, emphasising the potential importance of frequency-dependent reflection coefficients (Chapman et al. 2006, Odebeatu et al. 2006, Ren et al. 2009, Innanen 2011, Liu et al. 2018). Particularly, attention has been focused on the detection of fluid saturation. Wu et al. (2014) proposed a method to estimate gas saturation from pre-stack seismic data in a partially saturated sand based on frequency-dependent reflectivity and rock physics theory. Jin et al. (2017) extended the method to a thin-layer case by incorporating frequency-dependent reflectivity into convolutional modelling, which allows them to synthesize forward seismic

traces from well logs and investigate the effects of seismic dispersion on waveforms. These studies assumed the absence of fractures and therefore are limited to isotropic reservoirs.

In the presence of fractures, the use of anisotropic dispersion has shown potential for accurately characterizing fracture properties. However, the impact of FDA on azimuthal P-wave reflection appears to be less well understood; indeed a majority of studies take advantage of shear-wave splitting (e.g., Maultzsch et al. 2003a, Al-Harrasi et al. 2011) and attenuation (e.g., Chapman 2003, Chichinina et al. 2006, Liu et al. 2007, Wang et al. 2015, Ekanem et al. 2016). Moreover, most of current theories have been limited to the single fluid assumption, despite the fact that almost all reservoirs are partially saturated. Considering these issues, in this paper we investigate the impact of partial saturation on anisotropic P-wave dispersion using a theory developed by Jin et al. (2018), which quantitatively describes the coupled "squirt" and "patch" effects on FDA in a fractured rock saturated by two immiscible fluids. We also study how such effects influence azimuthal P-wave reflections, as deviations from the elastic assumption could potentially affect the interpretation of seismic data and the accuracy of fracture characterization.

In this paper, we develop a convolutional FDA modelling framework by extending the method of Jin et al. (2017) to anisotropic case and investigate the effects of FDA on azimuthal P-wave reflection based on an HTI sand model overlaid by an elastic shale. Our results suggest that the main impact of FDA is on azimuthal phase, and the presence of transverse isotropy with vertical symmetry axis (VTI) in the overlying shale could significantly affect the azimuthal behaviour of frequency-dependent AVO responses. Recognizing the impact of seismic dispersion in fractured media could potentially help differentiate between large-scale and micro-scale fractures.

We start by introducing the calculation of frequency-dependent reflection coefficient in partially saturated rock with aligned fractures modelled by the theory of Jin et al. (2018). We then review the convolutional modelling generalized by Jin et al. (2017) for the computation of synthetic seismic traces. We base the frequency-dependent azimuthal AVO study on the Class I model of Rutherford and Williams (1989) where we consider the overlying shale being either isotropic or anisotropic (VTI). Phase variations with both incidence angle and azimuth are particularly investigated. Finally, we consider a model-based Bayesian inversion to recover the water saturation, fracture density, and fracture length of the dispersive target. Our results show potential of using pre-stack reflection data to recover water saturation and to differentiate between large-scale and micro-scale fractures.

Methods

We calculate the reflection coefficient from Zoeppritz equations generalized by Schoenberg and Protazio (1992). Considering that the anisotropic medium has a horizontal plane of symmetry parallel to the $x_1 - x_2$ plane, let $x_3 = 0$ be the horizontal interface between two half spaces. We assume the horizontal components of slowness are all real (i.e., the source being placed in an elastic layer), and specify the incident wave with angle of incidence θ and azimuth φ. The direction of propagation can be expressed as

$$\mathbf{n} = \begin{bmatrix} \sin\theta\cos\varphi \\ \sin\theta\sin\varphi \\ \cos\theta \end{bmatrix}. \tag{1}$$

The slowness ξ of this incident wave is given by

$$\xi = \sqrt{\frac{\rho}{\chi}}, \tag{2}$$

where ρ is the density of the rock, and χ is the smallest eigenvalue of the matrix $c_{ijkl}n_i n_k$ (Chapman and Liu 2003) where c_{ijkl} represent the elements of the stiffness tensor. The horizontal slowness components s_1 and s_2 are therefore

$$s_1 = \xi \sin\theta \cos\varphi, \quad s_2 = \xi \sin\theta \sin\varphi. \tag{3}$$

Keeping s_1 and s_2 constant for all waves interacting at the interfaces, we then calculate the vertical slowness and polarizations of the ray in the dispersive medium by solving the Christoffel equation

$$|\rho\delta_{ik} - \Gamma_{ik}| = 0, \tag{4}$$

where δ_{ik} is the Kronecter parameter, and $\Gamma_{ik} = c_{ijkl}s_l s_j$ is defined as the Christoffel matrix. The eigenvalues of equation (4) are squared solutions of vertical slowness s_{3p}, s_{3s} and s_{3t} for quasi-P wave, the first arriving quasi-S wave and the last arriving quasi-S wave, respectively. The associated eigenvectors are corresponding polarizations $\mathbf{e_p}$, $\mathbf{e_s}$ and $\mathbf{e_t}$. With the solutions of vertical slowness, we can apply the continuities of displacement and traction at the interface $x_3 = 0$ to the wave equations to solve for the reflection coefficients corresponding to angle of incidence θ and azimuth φ from Zoeppritz equations generalized by Schoenberg and Protazio (1992).

We then describe the frequency-dependence of the reflection coefficient by using the theory of Jin et al. (2018), which is an extension of the model of Papageorgiou and Chapman (2017) to the anisotropic case. The theory models coupled "squirt" and "patch" effects on seismic anisotropy in a fractured rock saturated by two immiscible fluids. It considers the fractured rock as an effective medium consisting of an isotropic collection of grain-scale pores and cracks and a set of aligned meso-scale fractures. The resulting medium is transversely isotropic. During the passage of a seismic wave, the induced unrelaxed fluid pressure gradient between the inclusions gives rise to squirt flow. By considering the effect of relative permeability and

allowing for pressure variations between the two fluids, they derived the frequency-dependent stiffness tensor as

$$c_{ijkl}(\omega) = c^0_{ijkl} - \phi_p c^1_{ijkl}(\omega) - \varepsilon_c c^2_{ijkl}(\omega) - \varepsilon_f c^3_{ijkl}(\omega), \quad (5)$$

where ω is frequency, ϕ_p is the porosity of the spherical pores, ε_c is the microcrack density, and ε_f is the fracture density. The results are consistent with the form of Chapman (2003) in that c^0_{ijkl} is the isotropic elastic tensor of the mineral matrix specified by the lame parameters λ and μ. c^1_{ijkl}, c^2_{ijkl}, and c^3_{ijkl} are corrections associated with spherical pores, microcracks, and meso-scale fractures, respectively. These corrections would depend on the effective bulk modulus of the two-fluid mixture and two characteristic frequencies associated with grain-scale cracks and meso-scale fractures. Following Jin et al. (2018), the effective fluid bulk modulus K_f is derived as

$$\frac{1}{K_f} = \frac{S_w}{\tilde{q}K_w} + \frac{(1-S_w)q}{\tilde{q}K_g}; \tilde{q} = S_w + q(1-S_w), \quad (6)$$

where S_w is the water saturation, K_w and K_g are the bulk moduli of the saturating fluids. The subscripts w and g denote the fluid types. q is a non-dimensional parameter defined by Papageorgiou and Chapman (2017) that quantifies the variation of induced pressures between the two fluids. It lies within the range $\frac{K_g}{K_w} \leq q \leq 1$. $q = 1$ corresponds to the isostress condition in which the two fluids are mixed uniformly at a fine scale. This simplifies the effective fluid modulus as a Reuss average $\frac{1}{K_f} = \frac{S_w}{K_w} + \frac{1-S_w}{K_g}$ that is known as Wood's equation. Values less than 1 represent pressure variation within fluids which could give rise to the so-called "patch" effects. Particularly, at the extreme value $q_0 = \frac{K_g}{K_w}$, the effective fluid modulus can be expressed by the volume average $K_f = S_w K_w + (1-S_w)K_g$, which is often referred to as the Voigt approximation to the patchy-saturation upper bound.

The theory takes into account of the relative permeability effects on reducing the fluid mobility of the two-fluid mixture. This further lowers the microcrack-scale characteristic frequency ω_m and the fracture-scale characteristic frequency ω_f, which are two important parameters determining the frequency regime where dispersion occurs (equivalent to $\frac{1}{\tau}$ defined by Chapman (2003)). Following Jin et al. (2018), we can express the relationship between ω_m and ω_f by

$$\frac{\omega_f}{\omega_0'} = \frac{\omega_m}{\omega_0} = \frac{M_f}{M_w}, \tag{7}$$

$$\omega_f = \frac{\varsigma}{a_f}\omega_m, \tag{8}$$

where M_f is the effective fluid mobility that can be derived as

$$M_f = \frac{\kappa_w}{\tilde{q}}M_w + \frac{q\kappa_g}{\tilde{q}}M_g; \quad M_w = \frac{\kappa}{\eta_w}; \quad M_g = \frac{\kappa}{\eta_g}, \tag{9}$$

where η is the viscosity, κ is the absolute permeability, κ_w and κ_g are the relative permeabilities of water and gas.

In the above equations, ω_0 and ω_0' are the values of ω_m and ω_f at full water saturation, ς is the grain size that is assumed to be identified with the radii of the pore and cracks but much smaller than the fracture length a_f. We would therefore expect the fracture-scale ω_f to be smaller than the microcrack-scale ω_m. In this model, the patch parameter q, the relative permeability and the length of fractures all contribute to lowering the characteristic frequency, which could potentially lead to frequency-dependent anisotropy in the seismic frequency band. The reflection coefficient is therefore calculated to be frequency dependent and complex in this case.

Jin et al. (2017) proposed a method to incorporate frequency-dependent reflectivity into convolutional modelling for the calculation of synthetic angle-domain seismic traces.

Following Jin et al. (2017), in this paper we model seismic traces in the angle- and azimuth-time domains according to the equation

$$x(\theta, \varphi, t) = \mathcal{F}^{-1}[W(\omega)R(\theta, \varphi, \omega)], \tag{10}$$

where $W(\omega)$ is the source wavelet $w(t)$ in frequency domain, $R(\theta, \varphi, \omega)$ is the frequency-dependent reflection coefficient at the interface, and $\mathcal{F}^{-1}$ denotes the inverse Fourier transform.

Saturation effects on P-wave anisotropy

Jin et al. (2018) have studied the effects of patchy saturation and squirt dispersion on frequency-dependent S-wave anisotropy. They show that the influence of relative permeability and patchy saturation on lowering the characteristic frequency at intermediate saturations could lead to non-monotonic behaviour of S-wave splitting with respect to changes in water saturation. Here we study how such effects could also affect P-wave anisotropy based on a porous rock saturated by water and supercritical CO_2. The parameters are listed in Table 1, in which the bulk and shear moduli represent measurements in the absence of fractures.

Figure 1 displays the variation of quasi P-wave velocity with water saturation at various frequencies and patch parameters q. The propagation is along the direction of the fracture normal. In the low frequency limit, the uniform saturation ($q = 1$) case corresponds to an abrupt increase of P-wave velocity as it approaches full water saturation. The presence of patchy saturation tends to stiffen the rock, leading to a smoother variation of velocity with water saturation. In the high frequency limit (e.g. $100\omega_0'$), the dependence of P-wave velocity on water saturation becomes less significant, and the introduction of patchy saturation only slightly increases the velocity. At intermediate frequencies (e.g., ω_0'), however, we show non-

monotonic variation of P-wave velocity with water saturation. Conventionally, we might expect the introduction of gas to lead to a drop in P-wave velocity since gas has smaller bulk modulus and viscosity than water. Our results indicate that such velocity drop may not always occur as the effects of relative permeability and patchy saturation could significantly lower the characteristic frequency. This results in stronger dispersion at intermediate saturations, leading to higher P-wave velocity compared to that at full water saturation.

Figure 2 shows the variation of frequency-dependent quasi P-wave velocities with direction of propagation. For both full water saturation and partial saturation cases, quasi P-wave velocities show $\cos 4\theta$ angular variation at very high frequencies and $\cos 2\theta$ angular variation at lower frequencies. This is consistent with Thomsen (1995) and Chapman (2003). At zero water saturation, however, we may no longer observe the $\cos 4\theta$ angular variation even at very high frequencies (Figure 2d). While the introduction of CO_2 leads to a drop in P-wave velocity due to the stiffening effect of the two-fluid mixture (Figure 2b), the presence of patchy saturation gives rise to stronger dispersion which could make up such velocity drop (Figures 2a and 2c).

Table 1. The parameters of a fractured rock saturated by water and supercritical CO_2.

Dry frame bulk modulus (Pa)	1.40×10^{10}	Porosity	10%
Dry frame shear modulus (Pa)	7.29×10^{9}	Crack density	0.02
Mineral bulk modulus (Pa)	2.20×10^{10}	Fracture density	0.05
Mineral shear modulus (Pa)	9.31×10^{9}	Fracture length (m)	1
Solid density (kg/m^3)	2650	Aspect ratio	1.0×10^{-4}
Relative permeability of water	${S_w}^3$	Relative permeability of CO_2	$(1 - S_w)^2$
Water viscosity (Pa.s)	6.0×10^{-4}	CO_2 viscosity (Pa.s)	2.1×10^{-5}
Water density (kg/m^3)	1000	CO_2 density (kg/m^3)	240
Water bulk modulus (Pa)	2.4×10^{9}	CO_2 bulk modulus (Pa)	1.1×10^{7}

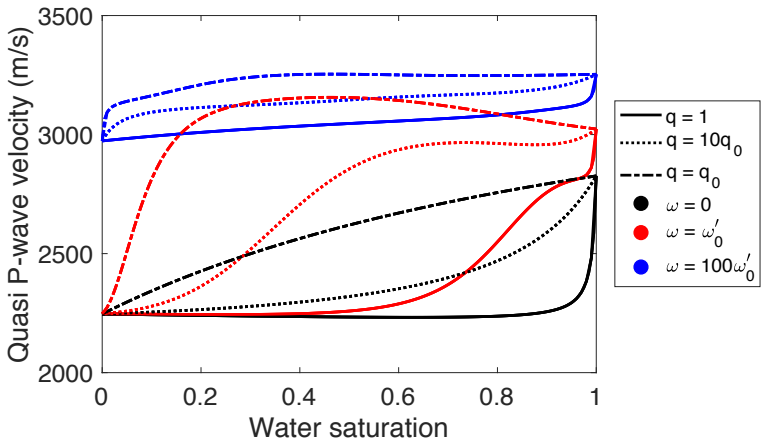

Figure 1. The variation of quasi P-wave velocity with water saturation for a range of patch parameters q and frequencies. The propagation is along the fracture normal.

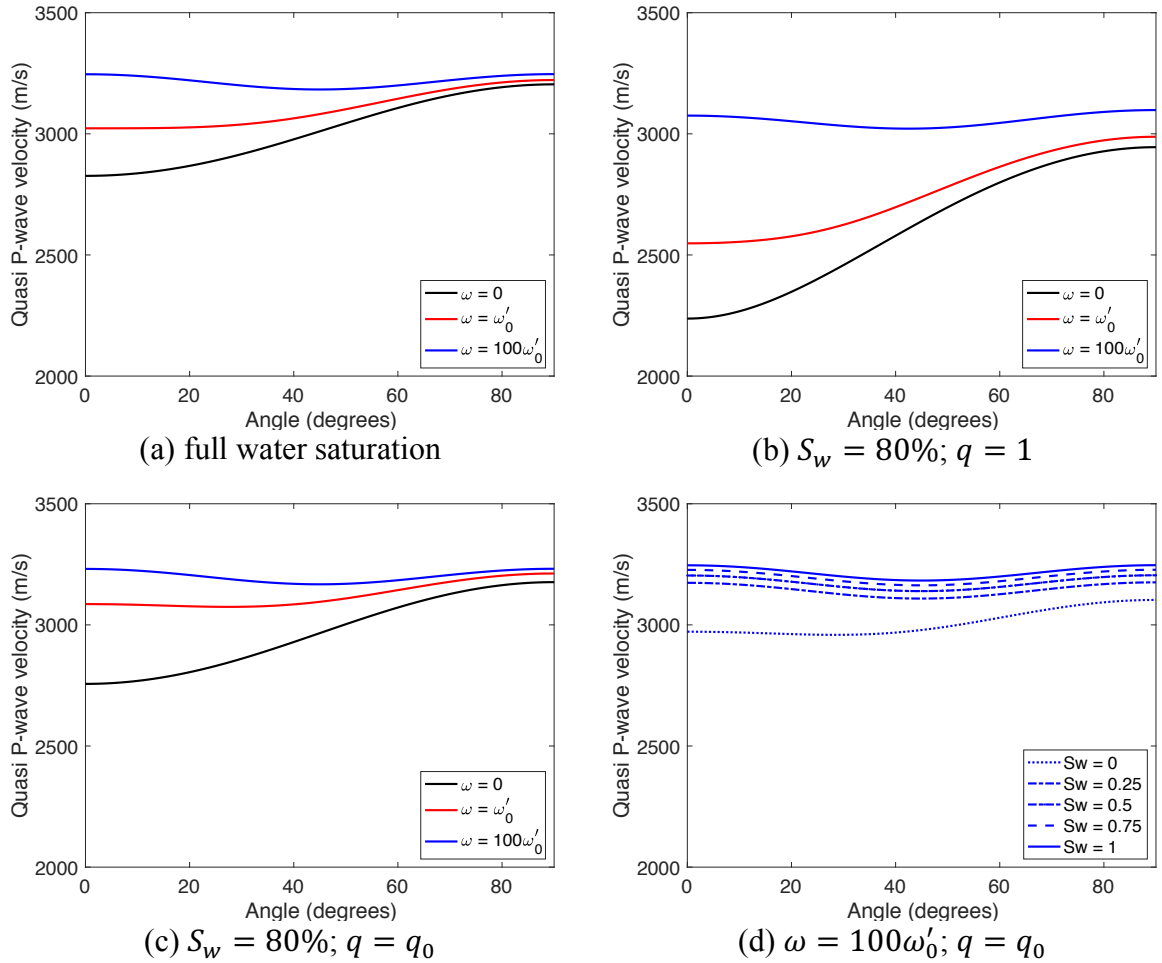

(a) full water saturation

(b) $S_w = 80\%;\ q = 1$

(c) $S_w = 80\%;\ q = q_0$

(d) $\omega = 100\omega_0';\ q = q_0$

Figure 2. The angular variation of quasi P-wave velocity for (a) the full water saturation case, (b) the 80% uniform saturation case with $q = 1$, (c) the 80% patchy saturation case with $q = q_0$, at various frequencies, and (d) the patchy saturation case with $q = q_0$ at very high frequency $100\omega_0'$.

Frequency-dependent azimuthal AVO

We study the effect of FDA on azimuthal P-wave reflection by considering the Class I example of Rutherford and Williams (1989). Table 2 displays the parameters for the model, which consists of a fractured sand reservoir overlaid by shale. We saturate the sand using the same fluids in Table 1. The velocities represent the measurements from the unfractured rock. We choose this model because Sayers and Rickett (1997) showed that the fractures have the strongest effect when the sand has higher acoustic impedance than the overlying shale. They investigated the azimuthal variation of AVO response based on this model by introducing anisotropy in the sand while assuming the shales being isotropic. They characterized the fractures by using the normal and tangential compliances Z_N and Z_T (Schoenberg and Sayers 1995), which allowed the calculation of frequency-independent reflectivity parallel and perpendicular to the strike of fractures. The results suggested that the effect of fractures only becomes noticeable at very large angles.

Table 2. The modified Class I model of Rutherford and Williams (1989) characterized by Thomsen's parameters and Jin et al. (2018) model.

Layers	Vp (m/s)	Vs (m/s)	Density (kg/m^3)	Elasticity	Model parameters			
Shale	3300	1700	2350	Elastic (Frequency-independent)	Thomsen's parameters (VTI)			
					$\epsilon = 0.1$	(a) $\delta = 0.1$ (b) $\delta = -0.1$		
Sand	4200	2700	2490	(a) Elastic (b) Frequency-dependent	Jin et al. (2018) model (HTI)			
					Porosity	Crack density	Fracture density	Fracture length (m)
					0.1	0.1	0.05	1

In reality, shale often shows intrinsic anisotropy due to preferentially alignment of clay particles. It is also known that the presence of large fractures in a reservoir often leads to FDA.

Under these circumstances, we consider scenarios where the elastic shale is transversely isotropic with vertical axis of symmetry (VTI) and the dispersive sand has vertically aligned fractures which show transverse isotropy with horizontal axis of symmetry (HTI). We use Thomsen's parameters ϵ and δ to characterize the VTI shale and use Jin et al. (2018) model to describe frequency-dependence of the HTI sand. Figure 3 shows the effects of VTI in the overlying shale on elastic azimuthal AVO curves under various Thomsen's parameters. Both shale and sand are assumed to be elastic. The blue solid curves represent the results for the isotropic overlying shale, which are consistent with Sayers and Rickett (1997). In the following studies, we characterize the VTI shale by using two sets of Thomsen's parameters $\epsilon = 0.1;\ \delta = 0.1$ and $\epsilon = 0.1;\ \delta = -0.1$ respectively and compare to the results based on the isotropic shale assumption.

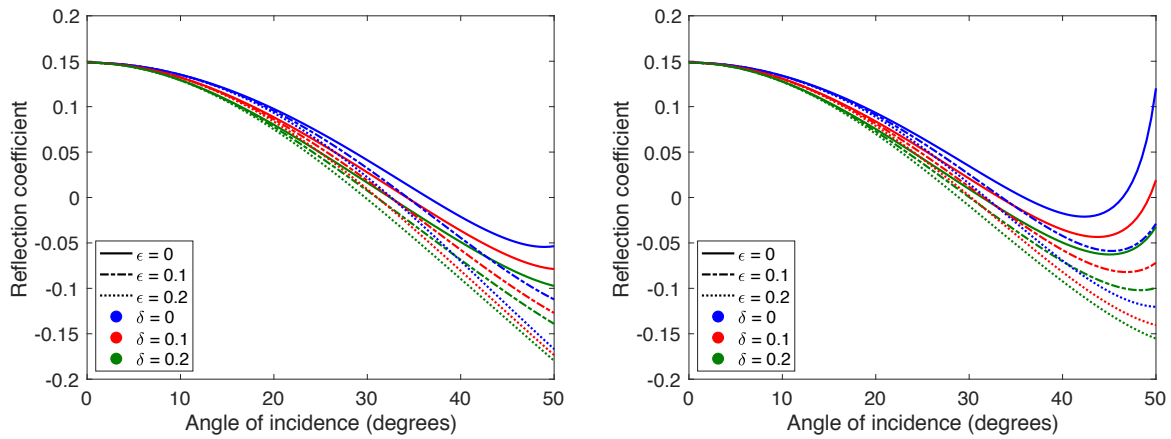

(a) 0-degree azimuth (b) 90-degree azimuth

Figure 3. Azimuthal AVO responses at an interface separated by VTI shale and HTI sand for a range of Thomsen's parameters. (a) The azimuth is 0 degree; (b) The azimuth is 90 degrees.

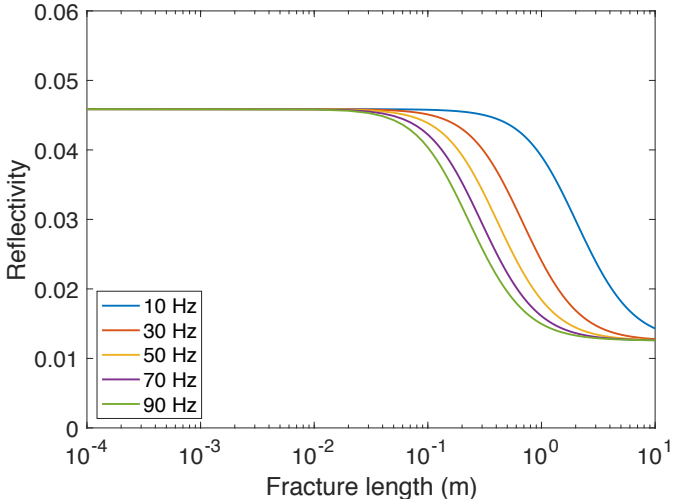

Figure 4. The impact of fracture length on frequency-dependent P-wave reflection at the interface between isotropic shale and fractured sand with HTI anisotropy. The angle of incidence is 45 degrees, and the azimuth is 0 degree.

Our approach of calculating reflection coefficient from Zoeppritz equations and Jin et al. (2018) theory allows the parameterisation of fracture density and fracture length. In current literature (e.g., Chapman 2003), the timescale parameter τ was used as 2×10^{-5} s, which corresponds to a characteristic frequency $\omega_0 = 5 \times 10^4$ Hz. Assuming the grain size $\varsigma = 2 \times 10^{-4}$ m and the fracture size $a_f = 1$ m, the fracture-scale characteristic frequency ω_0' is calculated as 10 Hz. We would therefore expect velocity dispersion to occur within the seismic frequency range in the presence of large fractures. The model by Jin et al. (2018) also suggests that the fracture length plays an important role in controlling the range where dispersion occurs. Figure 4 demonstrates this effect on frequency-dependent P-wave reflection by varying the fracture length in the sand from 0.1 mm to 10 m. The P-wave reflection is calculated at the incidence angle of 45 degrees and azimuth of 0 degree. For grain-scale microcracks (e.g., 1 mm), there is no dispersion in the seismic frequency range, and the fractured gas sand is equivalent to the elastic medium considered by Sayers and Rickett (1997). For large-scale fractures (e.g., 1 m), the gas sand exhibits strong FDA in the seismic frequency range.

To demonstrate the azimuthal dependence of P-wave reflections. We first consider the case where the fractured sand is elastic (i.e. frequency-independent microcrack case). Figure 5 displays the influence of VTI anisotropy in the overlying shale to the AVO responses for acquisitions with azimuth varying from 0 to 90 degrees. In the case of isotropic shale, the results are consistent with Sayers and Rickett (1997), where polarity changes of reflection occur at certain angles of incidence which we call reversal angles. The amplitude of reflectivity becomes zero and the phase jumps between 0 degree and 180 degrees discontinuously at the reversal point. The introduction of VTI influences the dependence of reflectivity on the angle of incidence (Rüger 1997, Tsvankin 2012). Figure 5b compares the AVO responses at zero azimuth for various Thomsen's parameters of the shale. The presence of VTI anisotropy changes both reversal angles and the far-offset reflectivities. Such difference can be well illustrated by the corresponding angle-domain seismic traces in Figure 8a where the source is a Ricker wavelet with 40 Hz peak frequency. The red line represents the location of the interface. Although VTI does not give rise to azimuthal anisotropy in the overlying shale, its effect on angle dependence could further affect the azimuthal anisotropy of AVO responses at the VTI-HTI interface. As a result, we may no longer observe the multiple polarity changes as the azimuthal angle increases (Figure 5c). Although our results in Figure 5a agree with Sayers and Rickett (1997) in that the azimuthal anisotropy only become noticeable at very large angles, the presence of VTI in the overlying shale could lead to a much weaker azimuthal variation of reflectivity compared to results based on the isotropic shale assumption (Figures 5d and 5e).

We now investigate the effects of frequency-dependence in the HTI sand on the azimuthal AVO responses. Both isotropic and VTI overlying shales are considered. Figure 6 displays the variation of P-P reflectivity, which is the norm of the complex-valued reflection coefficient, with angle of incidence and azimuth at various frequencies. Again, significant azimuthal effects

only occur at large angles of incidence. In the isotropic and VTI ($\epsilon = 0.1;\ \delta = -0.1$) shale cases shown in Figures 7a and 7b, the reflectivities at various frequencies do not reduce to zero, and the phase variations appear to be continuous. The corresponding pre-stack seismic traces therefore show strong phase variations with the increase of incidence angle (Figure 8b). The influence of dispersion is negligible at small angles. For angles larger than 30 degrees, a more gradual variation in both amplitude and phase can be observed from the frequency-dependent case. In comparison to results shown in Figures 7a and 7b, phase variation in the VTI ($\epsilon = 0.1;\ \delta = 0.1$) case (Figure 7c) becomes less significant at large angles, as we can hardly observe noticeable phase effects on the seismic traces shown in the bottom of Figure 8b.

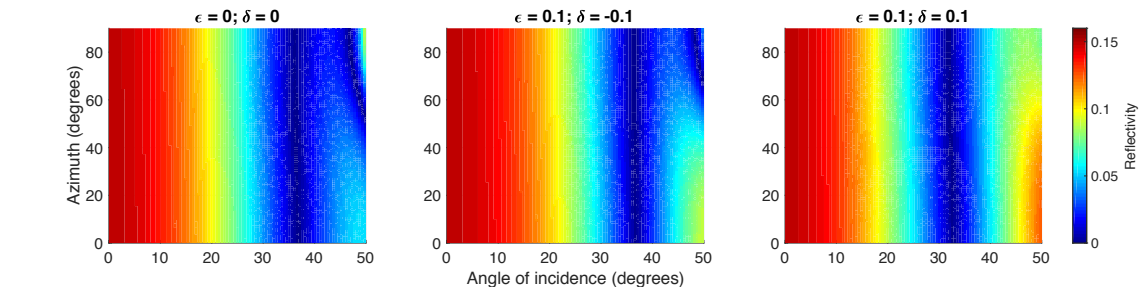

(a)

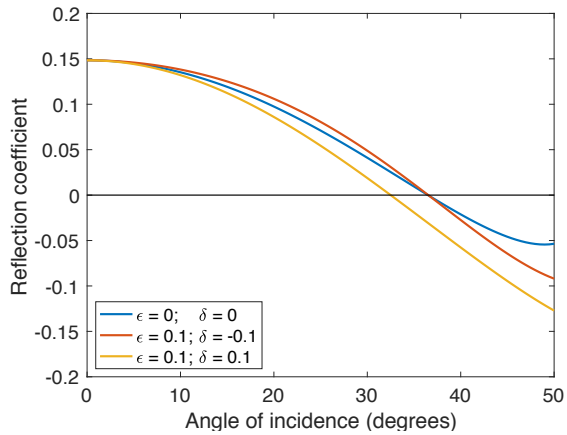

(b) 0-degree azimuth

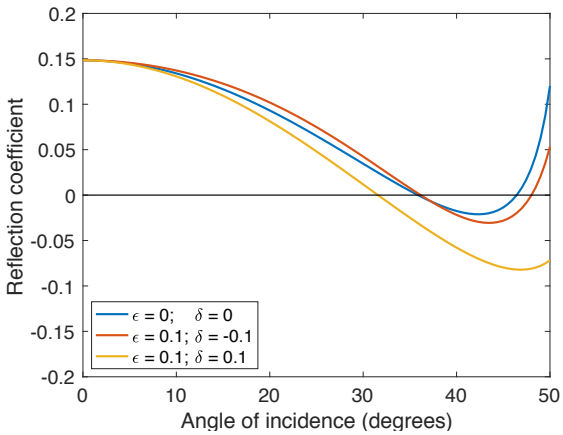

(c) 90-degree azimuth

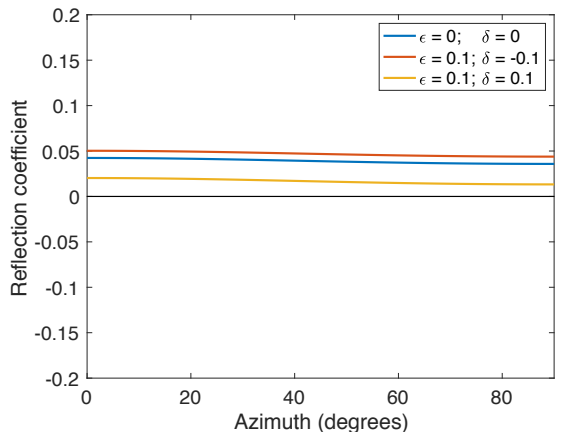

(d) 30-degree angle

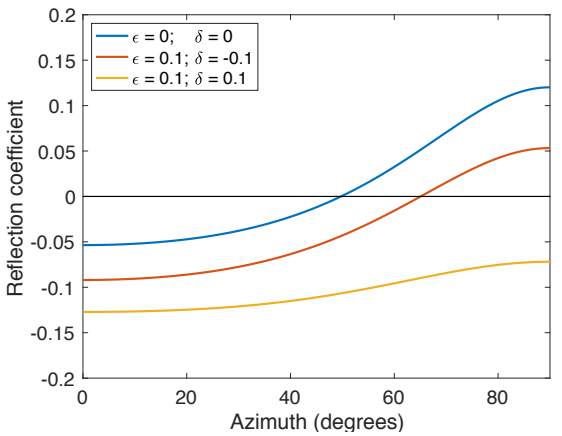

(e) 50-degree angle

Figure 5. (a) The variation of P-P reflectivity with angle of incidence and azimuth for a range of Thomsen's parameters of the VTI shale. (b) The variation of reflection coefficient with angle of incidence at 0-degree azimuth. (c) The variation of reflection coefficient with angle of incidence at 90-degree azimuth. (d) The variation of reflection coefficient with azimuth at 30-degree angle. (e) The variation of reflection coefficient with azimuth at 50-degree angle. The HTI sand is frequency independent.

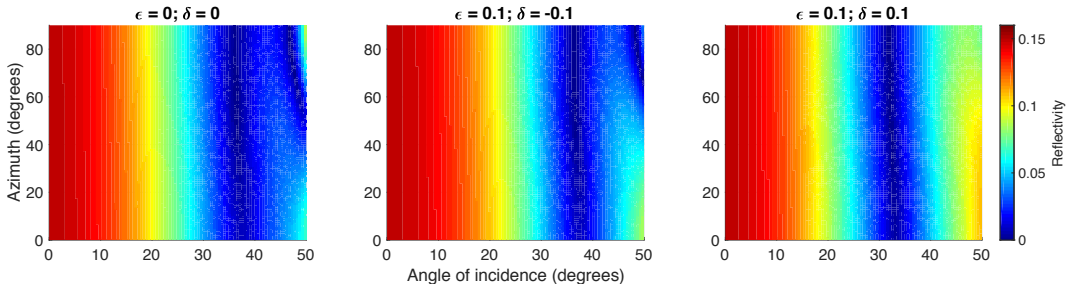

(a) 10 Hz

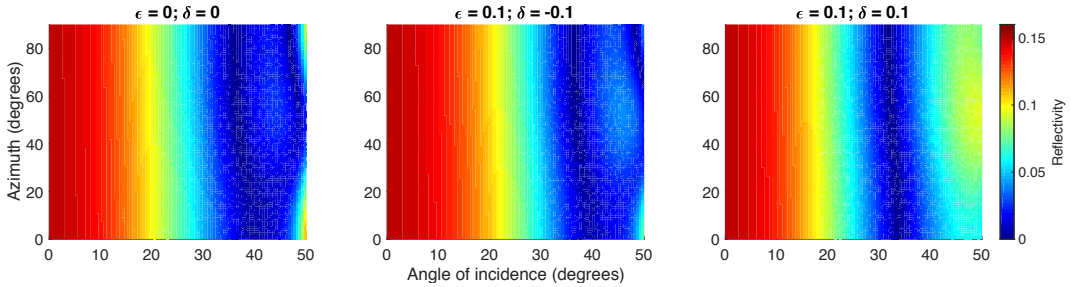

(b) 50 Hz

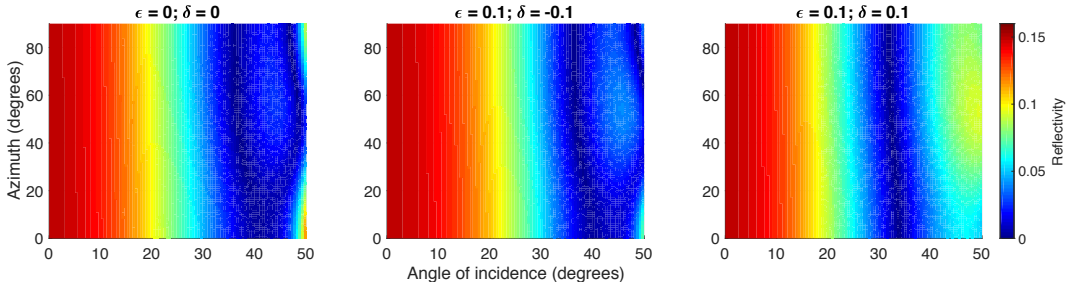

(c) 90 Hz

Figure 6. The variation of P-P reflectivity with angle of incidence and azimuth at the interface separated by VTI shale and frequency-dependent HTI sand for a range of frequencies at (a) 10 Hz (b) 50 HZ and (c) 90 Hz.

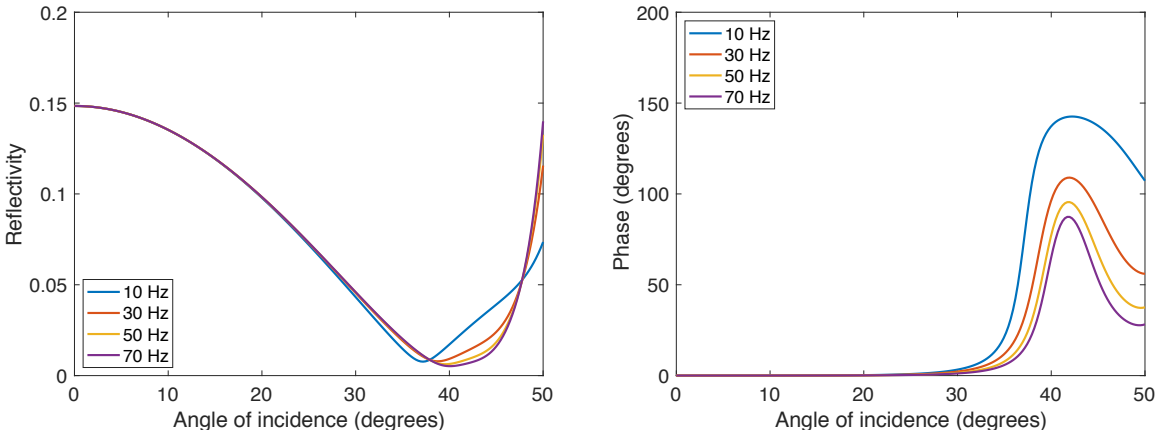

(a) isotropic shale $\epsilon = 0;\ \delta = 0$

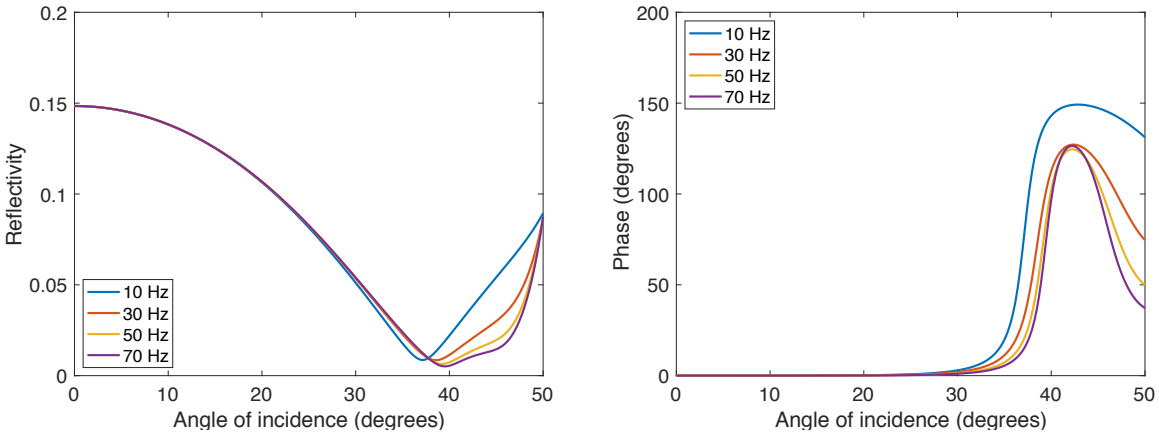

(b) VTI shale $\epsilon = 0.1;\ \delta = -0.1$

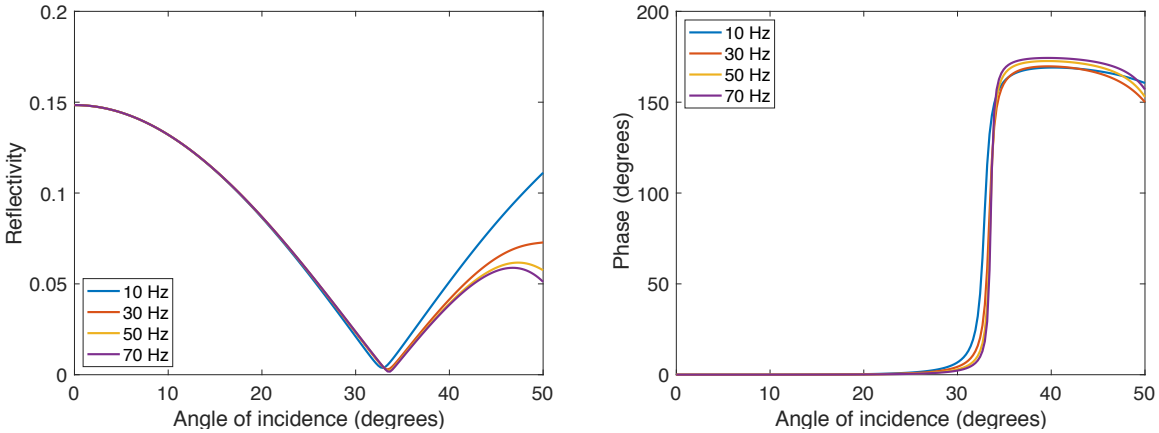

(c) VTI shale $\epsilon = 0.1;\ \delta = 0.1$

Figure 7. The frequency-dependent AVO curves and phase variations from acquisition perpendicular to fractures (zero azimuth) for (a) the isotropic shale case with $\epsilon = 0;\ \delta = 0$; (b) the VTI shale case with $\epsilon = 0.1;\ \delta = -0.1$; (c) the VTI shale case with $\epsilon = 0.1;\ \delta = 0.1$.

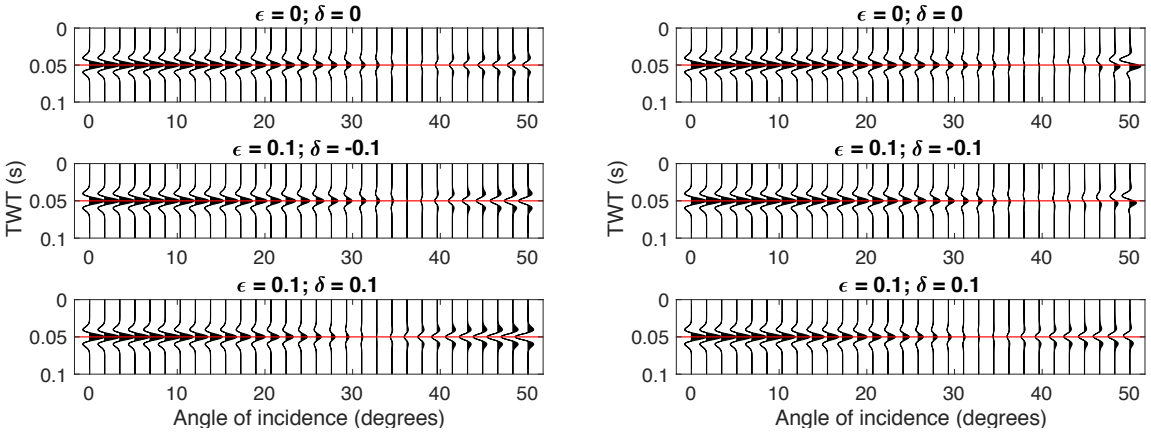

(a) elastic case (b) frequency-dependent case

Figure 8. The pre-stack angle domain seismic traces from acquisition perpendicular to fractures (zero azimuth) for (a) the frequency-independent HTI sand overlaid by VTI shale and (b) the frequency-dependent HTI sand overlaid by VTI shale. Various Thomsen's parameters are used to characterize the VTI shale. The red line represents the location of the interface.

Since the azimuthal variation becomes obvious only when the angle of incidence is large, now we take the angle as 50 degrees and demonstrate the elastic and frequency-dependent behaviours of P wave reflections as a function of azimuth in Figure 9. In the frequency-independent case (Figure 5a), polarity change occurs at the reversal azimuth where the amplitude reduces to zero and the phase jumps from 180 degrees to 0 degree. The introduction of dispersion leads to different behaviours regarding to phase reversal as Figures 9a and 9b demonstrate that the frequency-dependent reflection coefficient becomes non-zero and the phase varies continuously. Seismic dispersion is strong at small azimuths and becomes much weaker as the propagation approaches the direction parallel to fractures. This effect is clearly illustrated by comparing the azimuth-domain waveforms in Figures 10a and 10b. FDA plays an important role in reshaping the reflected waveforms in terms of amplitude and phase, and this phenomenon is particularly obvious for azimuth angles smaller than 60 degrees in this example.

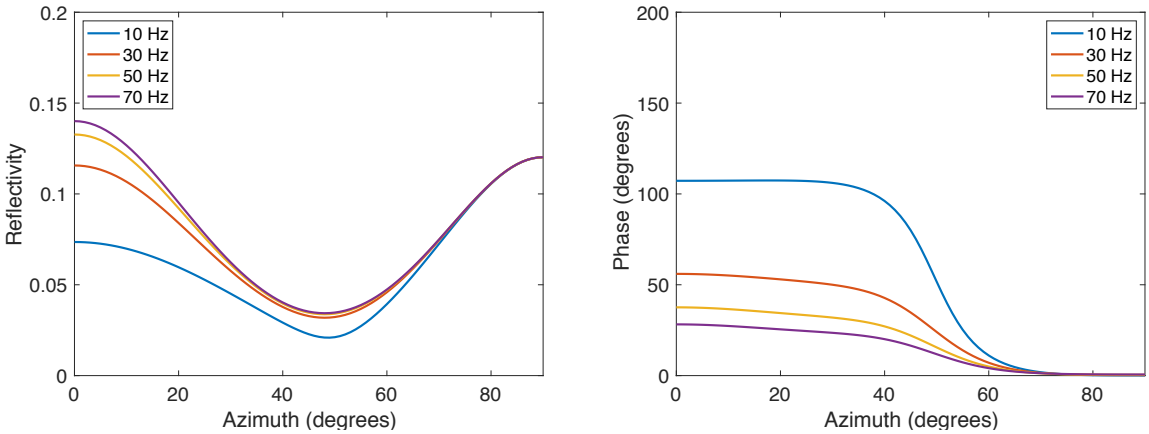

(a) isotropic shale $\epsilon = 0;\ \delta = 0$

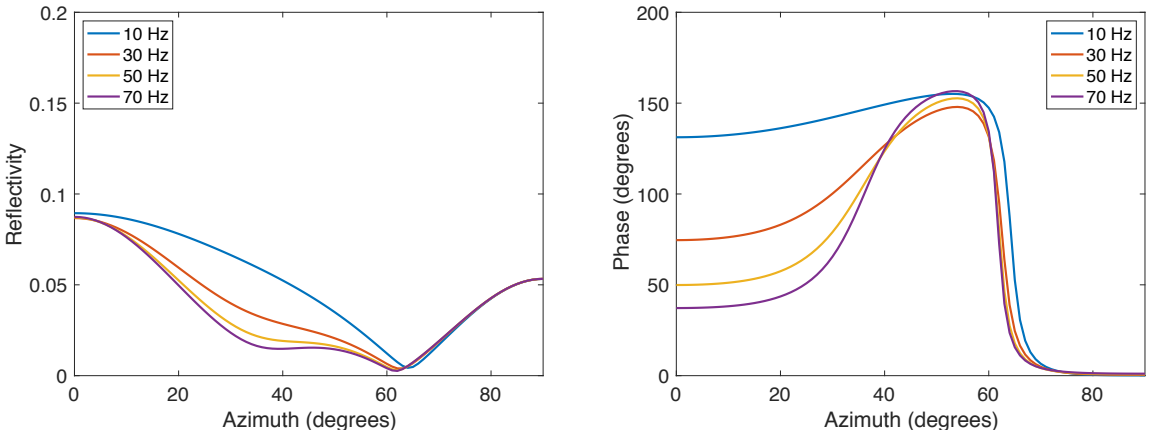

(b) VTI shale $\epsilon = 0.1;\ \delta = -0.1$

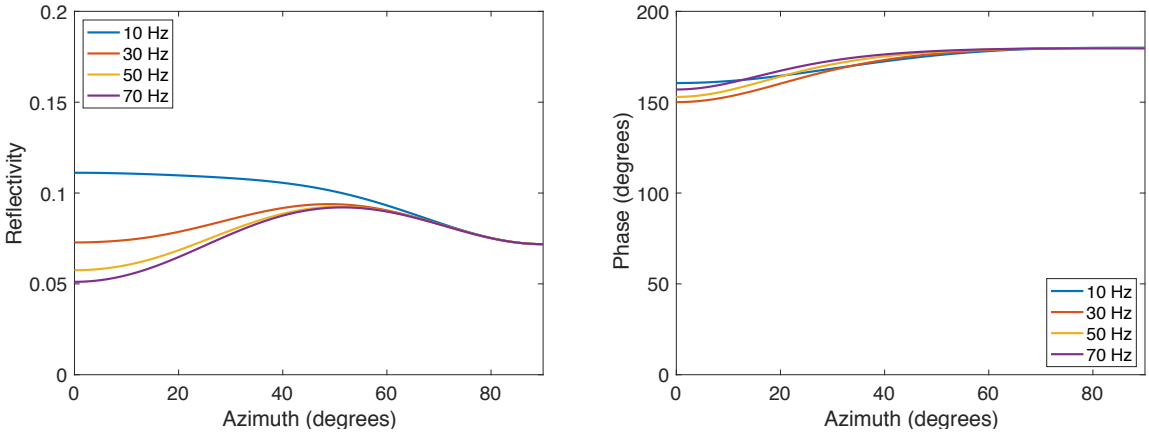

(c) VTI shale $\epsilon = 0.1;\ \delta = 0.1$

Figure 9. The frequency-dependent variation of reflectivities and phases with azimuth at 50-degree angle of incidence for (a) the isotropic shale case with $\epsilon = 0;\ \delta = 0$; (b) the VTI shale case with $\epsilon = 0.1;\ \delta = -0.1$; (c) the VTI shale case with $\epsilon = 0.1;\ \delta = 0.1$.

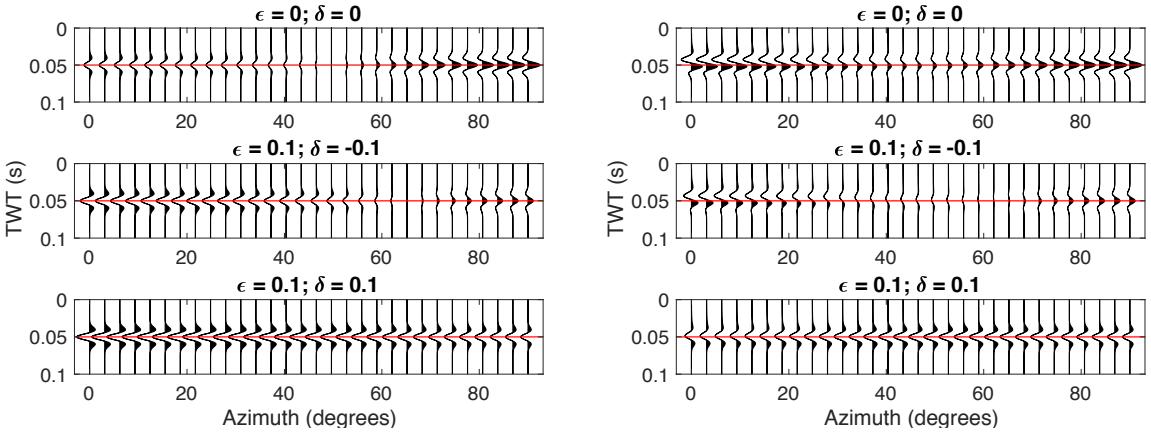

(a) elastic case (b) frequency-dependent case

Figure 10. The azimuth domain seismic traces from acquisition at 50-degree angle of incidence for (a) the frequency-independent HTI sand overlaid by VTI shale and (b) the frequency-dependent HTI sand overlaid by VTI shale. Various Thomsen's parameters are used to characterize the VTI shale. The red line represents the location of the interface.

We now consider the VTI shale being characterized by $\epsilon = 0.1;\ \delta = 0.1$. The reflectivity curves are shown in Figure 9c. In this case, polarity change can no longer be observed as the reflections are negative for all azimuths. The introduction of seismic dispersion in the HTI sand leads to weaker amplitudes of reflected waves (comparing Figures 10a and 10b), but minimal phase effects can be expected on the reflected waveforms as suggested by the phase curves in Figure 9c. The presence of VTI in the overlying shale could therefore significantly change the azimuthal behaviour of frequency-dependent AVO responses in terms of both amplitude and phase variations.

We further investigate the potential impacts of azimuthal phase effects on amplitude and apparent arrival time. We do this by considering the VTI shale case with $\epsilon = 0.1;\ \delta = -0.1$ where phase reversal occurs. Figure 11 displays the amplitude picking results from the first horizon. For the elastic case in Figure 11a, the picked amplitude at each azimuth fits well with the reflection coefficient curve at zero frequency, and clearly approaches zero when the azimuth is around 60 degrees. For the frequency-dependent case in Figure 11b, the amplitudes vary more gradually and never reduce to zero. They are approximately proportional to the

reflection coefficients at the peak frequency. In the elastic case, the peak locates exactly in the horizon, while in the FDA case there is a difference which we refer to as the apparent azimuthal residual. Figure 12 shows this apparent azimuthal residual between the time depths of the waveform peak and the first horizon. We note that failure to recognize this effect during velocity analysis could potentially give rise to incorrect estimate of azimuthal velocity variations.

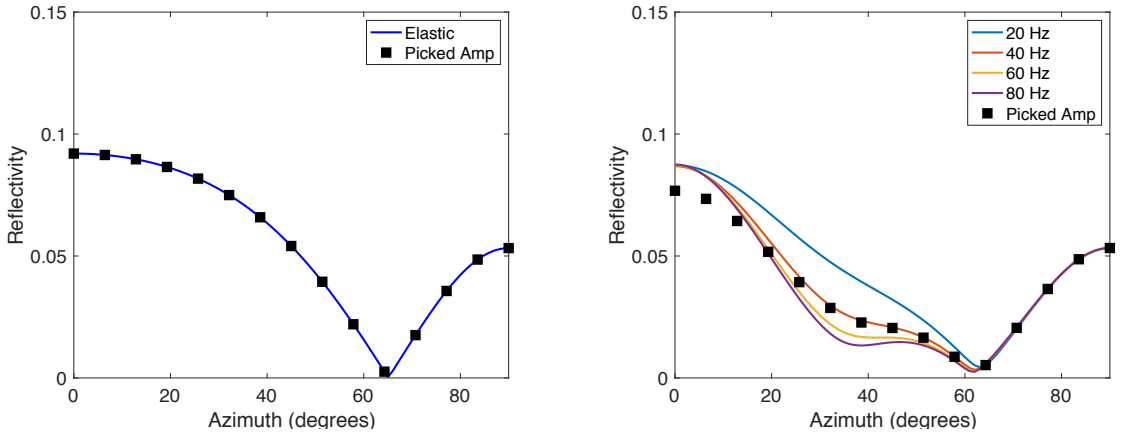

(a) (b)

Figure 11. The amplitude picking of azimuth-domain seismic traces for (a) the elastic case and (b) the frequency-dependent case. The angle of incidence is 50 degrees. Curves represent the reflection coefficients. Squares represent the picked amplitudes.

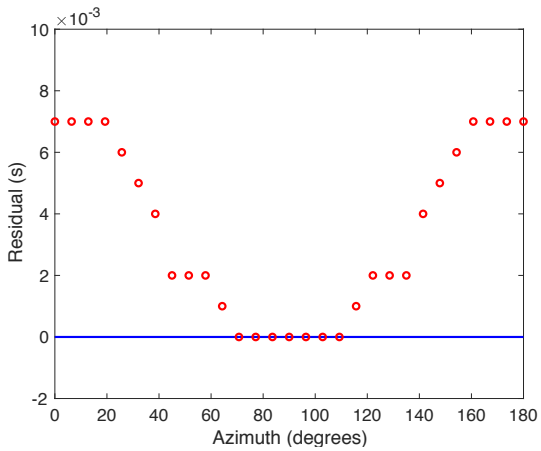

Figure 12. The variation of traveltime residual with azimuth for the seismic traces shown in Figure 10 ($\epsilon = 0.1;\ \delta = -0.1$). The blue line indicates the residual for the elastic case. The red circle represents the residual for the frequency-dependent case.

Bayesian inversion for fluid and fracture properties

Bayesian inversion has been widely used for estimating rock properties from seismic data (Mavko and Mukerji 1998, Spikes et al. 2007, Wu et al. 2014). Jin et al. (2017) proposed a Bayesian scheme aimed at recovering water saturation from pre-stack seismic data using a modelling technique that incorporates frequency-dependent reflection coefficients. In this paper, we extend previous technique to anisotropic case with a particular focus on the estimation of water saturation, fracture density, and fracture length. We consider a single interface example with the upper layer being VTI shale and the lower layer being a partially saturated sand with aligned vertical fractures. Based on the inversion scheme proposed by Jin et al. (2017), the main steps in this study are as follows:

(i) Forward modelling the seismic trace $f(s_w, \varepsilon_f, a_f)$, as written from equation (10), for various values of water saturation s_w, fracture density ε_f and fracture length a_f by assuming all other background parameters are known.

(ii) Calculating the misfits between the observed data d (pre-stack seismic traces) and the forward model responses at $(s_w, \varepsilon_f, a_f)$ by using equation

$$\Delta E = \sum \left\| d - f(s_w, \varepsilon_f, a_f) \right\|_2. \tag{11}$$

(iii) Calculating the likelihood function $P\left(d \middle| s_w, \varepsilon_f, a_f\right)$ from exponentially transforming the misfit:

$$P\left(d \middle| s_w, \varepsilon_f, a_f\right) \propto \exp\left(-b \cdot \Delta E\right), \tag{12}$$

where b is a constant, the determination of which has been discussed by Jin et al. (2017). In this paper, we choose value of 20 for illustration purposes.

(iv) Obtaining prior information $P(s_w, \varepsilon_f, a_f)$ from well-log analysis, and the posterior probability of inversion targets s_w, ε_f, and a_f can be calculated by

$$P(s_w, \varepsilon_f, a_f|d) = \frac{P(d|s_w,\varepsilon_f,a_f)P(s_w,\varepsilon_f,a_f)}{P(d)}, \tag{13}$$

where $P(d)$ is a constant that normalizes the final results.

We use same parameters in Table 2 to perform a synthetic study. The overlying VTI shale is characterized by Thomsen's parameters $\epsilon = 0.1;\ \delta = -0.1$. The HTI sand is saturated by 60% water and 40% CO_2, and the patch parameter q is assumed to be $10q_0$. We consider two fracture cases with the same density 0.05 but different sizes, i.e., grain-scale with length of 1 mm and meso-scale with length of 1 m. Figure 13 shows the pre-stack data in both angle and azimuth domain with 10% Gaussian noise added to the synthetic seismic traces computed by equation (10).

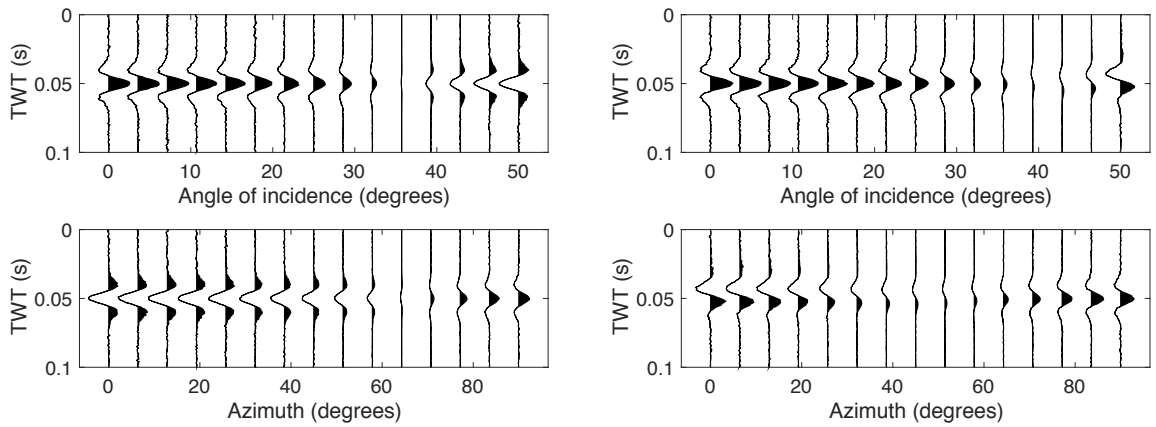

(a) micro-scale crack (b) meso-scale fracture

Figure 13. Synthetic angle- and azimuth-domain seismic data for (a) the microcrack case and (b) the meso-scale fracture case. For the angle-domain data, the acquisition is at zero azimuth. For the azimuth-domain data, the angle of incidence is fixed at 50 degrees.

Following the above steps, we first derive the forward seismic model as a function of s_w, ε_f, and a_f assuming that all other parameters are known. The likelihood function can then be obtained from the misfits between the observed data and model responses by scanning through the combinations of s_w, ε_f, and a_f. Assuming a unit probability distribution $P(s_w, \varepsilon_f, a_f)$ as prior information, we can finally calculate the posterior probability distribution $P(s_w, \varepsilon_f, a_f|d)$ from equation (13).

Figure 14 displays the marginal distribution of the posterior probability $P(s_w, \varepsilon_f, a_f|d)$ for the grain-scale crack and large-scale fracture cases, respectively. It is clear that these two cases can be well distinguished. The fracture length for the large-scale case is accurately recovered, while a range of lengths smaller than 1 cm appear to satisfy the micro-scale case. This is because seismic dispersion is controlled by the fracture size, and could be negligible as the size approaches grain-scale. The effects of seismic dispersion associated with large-scale fractures also contribute to an accurate estimation of water saturation and fracture density. However, for the micro-scale crack case where seismic dispersion is negligible, it is unlikely to accurately recover the water saturation. Figure 15 shows the estimation of s_w and a_f at fixed $\varepsilon_f = 0.05$. The results demonstrate that a more accurate estimation of water saturation can be achieved if we can effectively constrain the model. The consideration of seismic dispersion in azimuthal AVO analysis has therefore shown potential of discriminating large-scale fractures from micro-scale cracks.

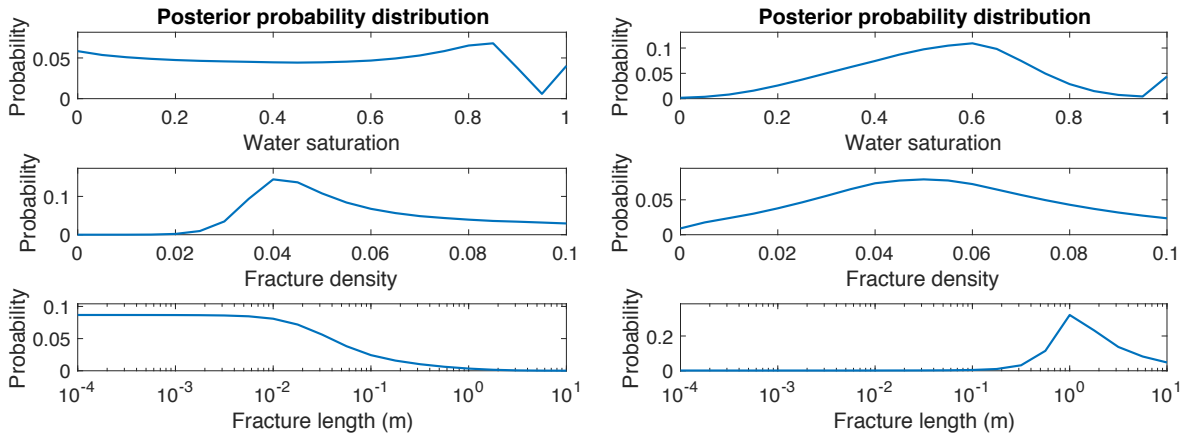

(a) micro-scale crack (b) meso-scale fracture

Figure 14. Marginal distribution of the posterior probability for water saturation, fracture density, and fracture length, respectively. (a) The microcrack case with true fracture length 1 mm; (b) The large-scale fracture case with true fracture length 1 m.

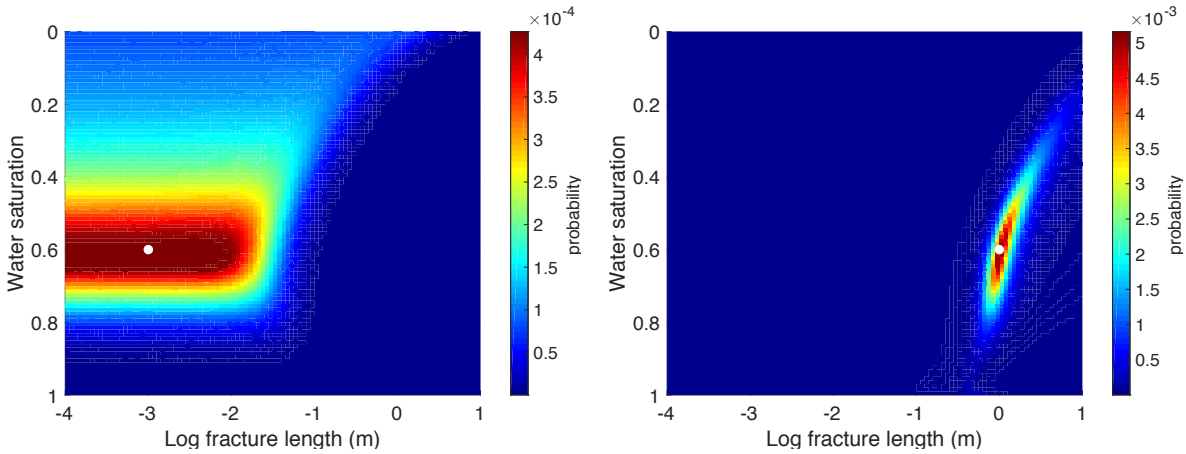

(a) (b)

Figure 15. The estimation of water saturation and fracture length based on the fracture density being determined as 0.05. (a) The microcrack case; (b) The large-scale fracture case. The true fracture length and water saturation is marked with white circle.

Discussion

The potential importance of FDA to seismic fracture characterization is clear. Techniques based on shear-wave splitting have been particularly studied, while less attention has been paid to the impacts of fracture-related dispersion on P-wave reflections. In this paper, we examined the effect of FDA on azimuthal P-wave reflection based on a forward convolutional modelling

strategy and a specific rock physics theory. According to the theories of Chapman (2003) and Jin et al. (2018), the frequency regime where the fracture-related dispersion occurs is determined by the length scale of the fractures and a timescale parameter τ (or characteristic frequency ω_0) that is directly related with fluid mobility. The behaviour of seismic dispersion is controlled by the value of τ, the impact of which on FDA has been studied by Maultzsch et al. (2003a). In our numerical example, we only choose $\tau = 2 \times 10^{-5}$ as used in Chapman (2003), although other values have also been considered in current literature (e.g. Amalokwu et al. 2016) for FDA inversions. In a real data application, τ acts as a parameter that has to be calibrated from available wells (Wu et al. 2014).

The fractured sand layer described by Chapman (2003) theory is modelled as an HTI medium, which contains only one set of aligned fractures in an isotropic background. Although considering such a model is simple and sufficient to model azimuthal anisotropy, fractured reservoirs can be orthorhombic and even triclinic in the presence of multiple sets of fractures (Grechka and Kachanov 2006a,b; Tsvankin and Grechka 2011), the influence of which on FDA would be worth investigating in future research since a lower symmetry could complicate both angle and azimuth dependences of seismic reflections.

The forward modelling method by Jin et al. (2017) calculates waveforms only based on frequency-dependent P-P reflection coefficients. The use of such a convolutional model with anisotropic reflectivity to interpret azimuthal amplitude variations is simple and convenient, but potentially problematic. Anisotropy in the overburden can lead to distortions in the amplitudes from transmission, spreading and attenuation (Maultzsch et al., 2003b), and these are not accounted for in the modelling. Methods which can be applied to data to correct for such effects have been discussed by Tsvankin (1995) and Xu and Tsvankin (2006).

In the numerical example presented, frequency-dependent effects on azimuthal AVO become significant at wide angles of incidence where azimuthal phase reversal occurs. The variation of amplitude with azimuth does not deviate far from corresponding reflection coefficients calculated from anisotropic Zoeppritz equations, but the phase variation could become obvious as the apparent azimuthal traveltime residuals are non-zero due to the presence of FDA. We demonstrate this by using only one model in which the overlying VTI shale is characterized by Thomsen's parameters $\epsilon = 0.1;\ \delta = -0.1$. It should be noted that such azimuthal phase variations should also be expected in other models such as an isotropic overlying shale as long as the phase reversal occurs. Such effects could be mistaken for azimuthal moveout, which may have implications for seismic velocity analysis.

The fracture length in reservoirs is usually several centimetres to meters, which is much larger than the length of the micro-scale cracks. While the inversion for microcracks may not be relevant to seismic exploration, we do this to show the discrimination between these two scales. The study of fracture-induced dispersive effects on AVO responses can be considered as an extension of previous technique by Jin et al. (2017) to anisotropic case. Current inversion scheme by Jin et al. (2017) was based on an idealized forward convolutional modelling and might not be realistic for immediate practical application. Nevertheless, the technique incorporates frequency-dependent reflectivities and could in principle handle more complex models (e.g. multiple layers). The numerical results indicate potential importance of our concepts to interpretation of azimuthal seismic response in field data, and application to particular datasets will form the focus of future work. Workflows for field data application of isotropic FAVO techniques have been presented by Wu et al. (2014). Robust inversion methods

for fracture characterization from seismic reflections would require appropriate regularization strategies which will be addressed in future research.

Conclusions

We have studied the effect of frequency-dependent anisotropy on azimuthal AVO response in a fractured Class I HTI sand overlaid by VTI shale. For acquisitions perpendicular to fractures, the frequency-dependent AVO behaviour shows a gradual continuous phase variation in contrast to the discontinuous phase reversal from the elastic case. The principal qualitative difference between frequency-dependent and frequency-independent responses lies in the azimuthal phase variation at wide angles of incidence. Such difference is visible on the synthetic seismograms calculated from a generalised convolutional modelling. We show modest effects on the picked amplitude but large effects on the apparent azimuthal traveltime residual. Failure to recognize this effect during velocity analysis could potentially give rise to incorrect estimate of azimuthal velocity variations. Fracture-induced dispersion influences both amplitude and phase variations of the interfering reflections, leading to the possibility of using frequency-dependent azimuthal AVO to distinguish between micro-cracks and large-scale fractures.

Acknowledgements

Zhaoyu Jin was supported by the Principal's Career Development PhD Scholarships and Edinburgh Global Research Scholarship from The University of Edinburgh. Mark Chapman and Xiaoyang Wu were partially supported by the Edinburgh Anisotropy Project (EAP), British Geological Survey. Giorgos Papageorgiou acknowledges financial support from the program PETROMAKS2 of the Research Council of Norway (RCN grant number: 267765).

References

Al-Harrasi, O.H., Kendall, J.M. and Chapman, M., 2011. Fracture characterization using frequency-dependent shear wave anisotropy analysis of microseismic data. *Geophysical Journal International*, *185*(2), pp.1059-1070.

Amalokwu, K., Best, A.I. and Chapman, M., 2016. Effects of aligned fractures on the response of velocity and attenuation ratios to water saturation variation: A laboratory study using synthetic sandstones. *Geophysical Prospecting*, *64*(4), pp.942-957.

Brajanovski, M., Gurevich, B. and Schoenberg, M., 2005. A model for P-wave attenuation and dispersion in a porous medium permeated by aligned fractures. *Geophysical Journal International*, *163*(1), pp.372-384.

Chapman, M., 2003. Frequency-dependent anisotropy due to meso-scale fractures in the presence of equant porosity. *Geophysical Prospecting*, *51*(5), pp.369-379.

Chapman, M. and Liu, E., 2003. The frequency dependent azimuthal AVO response of fractured rock. In *2003 SEG Annual Meeting*. Society of Exploration Geophysicists.

Chapman, M., Liu, E. and Li, X.Y., 2006. The influence of fluid sensitive dispersion and attenuation on AVO analysis. *Geophysical Journal International*, *167*(1), pp.89-105.

Chapman, M., 2009. Modeling the effect of multiple sets of mesoscale fractures in porous rock on frequency-dependent anisotropy. *Geophysics*, *74*(6), pp.D97-D103.

Chesnokov, E.M., Queen, J.H., Vichorev, A., Lynn, H.B., Hooper, J., Bayuk, I., Castagna, J. and Roy, B., 2001, September. Frequency dependent anisotropy. In *71st SEG Meeting, San Antonio, Texas, USA, Expanded Abstracts* (pp. 2120-2123).

Chichinina, T., Sabinin, V. and Ronquillo-Jarillo, G., 2006. QVOA analysis: P-wave attenuation anisotropy for fracture characterization. *Geophysics*,*71*(3), pp.C37-C48.

Collet, O. and Gurevich, B., 2016. Frequency dependence of anisotropy in fluid saturated rocks–Part I: aligned cracks case. *Geophysical Prospecting*, *64*(4), pp.1067-1084.

Ekanem, A.M., Li, X.Y., Chapman, M. and Main, I.G., 2016. Effects of CO 2 on P-wave attenuation in porous media with micro-cracks: A synthetic modelling study. *Journal of Applied Geophysics*, *135*, pp.309-316.

Grechka, V. and Kachanov, M., 2006a. Seismic characterization of multiple fracture sets: Does orthotropy suffice?. *Geophysics*, *71*(3), pp.D93-D105.

Grechka, V. and Kachanov, M., 2006b. Effective elasticity of fractured rocks: A snapshot of the work in progress. *Geophysics*, *71*(6), pp.W45-W58.

Guo, J., Rubino, J.G., Glubokovskikh, S. and Gurevich, B., 2017. Effects of fracture intersections on seismic dispersion: theoretical predictions versus numerical simulations. *Geophysical Prospecting*, *65*(5), pp.1264-1276.

Gurevich, B., 2003. Elastic properties of saturated porous rocks with aligned fractures. *Journal of Applied Geophysics*, *54*(3), pp.203-218.

Hall, S.A. and Kendall, J.M., 2003. Fracture characterization at Valhall: Application of P-wave amplitude variation with offset and azimuth (AVOA) analysis to a 3D ocean-bottom data set. *Geophysics*, *68*(4), pp.1150-1160.

Hudson, J.A., 1981. Wave speeds and attenuation of elastic waves in material containing cracks. *Geophysical Journal International*, *64*(1), pp.133-150.

Innanen, K.A., 2011. Inversion of the seismic AVF/AVA signatures of highly attenuative targets. *Geophysics*, *76*(1), pp.R1-R14.

Jakobsen, M. and Chapman, M., 2009. Unified theory of global flow and squirt flow in cracked porous media. *Geophysics*, *74*(2), pp.WA65-WA76.

Jin, Z., Chapman, M., Wu, X. and Papageorgiou, G., 2017. Estimating gas saturation in a thin layer by using frequency-dependent amplitude versus offset modelling. *Geophysical Prospecting*, *65*(3), pp.747-765.

Jin, Z., Chapman, M. and Papageorgiou, G., 2018. Modelling the effect of partial saturation on shear wave anisotropy. To appear in *SEG Technical Program Expanded Abstracts 2018*.

Liu, E., Hudson, J.A. and Pointer, T., 2000. Equivalent medium representation of fractured rock. *Journal of Geophysical Research: Solid Earth*, *105*(B2), pp.2981-3000.

Liu, E., Chapman, M., Zhang, Z., and Queen, J. H., 2006. Frequency-dependent anisotropy: Effects of multiple fracture sets on shear-wave polarizations. *Wave motion*, *44*(1), 44-57.

Liu, E., Chapman, M., Varela, I., Li, X., Queen, J.H. and Lynn, H., 2007. Velocity and attenuation anisotropy: Implication of seismic fracture characterizations. *The Leading Edge*, *26*(9), pp.1170-1174.

Liu, W., Cao, S., Jin, Z., Wang, Z. and Chen, Y., 2018. A Novel Hydrocarbon Detection Approach via High-Resolution Frequency-Dependent AVO Inversion Based on Variational Mode Decomposition. *IEEE Transactions on Geoscience and Remote Sensing*. 56(4), 2007-2024.

Lynn, H.B., Simon, K.M., Bates, C.R., Layman, M., Schneider, R. and Jones, M., 1995. Use of anisotropy in P-wave and S-wave data for fracture characterization in a naturally fractured gas reservoir. *The Leading Edge*, *14*(8), pp.887-893.

Marson-Pidgeon, K. and Savage, M.K., 1997. Frequency-dependent anisotropy in Wellington, New Zealand. *Geophysical Research Letters*, *24*, pp.3297-3300.

Maultzsch, S., Chapman, M., Liu, E. and Li, X.Y., 2003a. Modelling frequency-dependent seismic anisotropy in fluid-saturated rock with aligned fractures: implication of fracture size estimation from anisotropic measurements. *Geophysical Prospecting*, *51*(5), pp.381-392.

Maultzsch, S., Horne, S., Archer, S. and Burkhardt, H., 2003b. Effects of an anisotropic overburden on azimuthal amplitude analysis in horizontal transverse isotropic media. *Geophysical Prospecting*, *51*(1), pp.61-74.

Mavko G. and Mukerji T. 1998. A rock physics strategy for quantifying uncertainty in common hydrocarbon indicators. *Geophysics 63*(6), 1997-2008.

Odebeatu, E., Zhang, J., Chapman, M., Liu, E. and Li, X.Y., 2006. Application of spectral decomposition to detection of dispersion anomalies associated with gas saturation. *The Leading Edge*, *25*(2), pp.206-210.

Papageorgiou, G. and Chapman, M., 2017. Wave-propagation in rocks saturated by two immiscible fluids. *Geophysical Journal International*, *209*(3), pp.1761-1767.

Ren, H., Goloshubin, G. and Hilterman, F.J., 2009. Poroelastic analysis of amplitude-versus-frequency variations. *Geophysics*, *74*(6), pp.N41-N48.

Rüger, A., 1997. P-wave reflection coefficients for transversely isotropic models with vertical and horizontal axis of symmetry. *Geophysics*, *62*(3), pp.713-722.

Rüger, A., 1998. Variation of P-wave reflectivity with offset and azimuth in anisotropic media. *Geophysics*, *63*(3), pp.935-947.

Rutherford, S.R. and Williams, R.H., 1989. Amplitude-versus-offset variations in gas sands. *Geophysics*, *54*(6), pp.680-688.

Sayers, C.M. and Rickett, J.E., 1997. Azimuthal variation in AVO response for fractured gas sands. *Geophysical Prospecting*, *45*(1), pp.165-182.

Schoenberg M. and Protazio J. 1992. 'Zoeppritz' rationalized and generalized to anisotropy. Journal of Seismic Exploration 1, 125-144.

Schoenberg, M. and Sayers, C.M., 1995. Seismic anisotropy of fractured rock. *Geophysics*, *60*(1), pp.204-211.

Spikes K., Mukerji T., Dvorkin J. and Mavko G. 2007. Probabilistic seismic inversion based on rock-physics models. *Geophysics 72*(5), R87-R97.

Tsvankin, I., 1995. Body-wave radiation patterns and AVO in transversely isotropic media. *Geophysics*, *60*(5), pp.1409-1425.

Tsvankin, I. and Grechka, V., 2011. *Seismology of azimuthally anisotropic media and seismic fracture characterization* (pp. 372-382). Tulsa, OK: Society of Exploration Geophysicists.

Tsvankin, I., 2012. Seismic Signatures and Analysis of Reflection Data in Anisotropic Media Third Edition.

Wang, Y., Chen, S. and Li, X.Y., 2015. Anisotropic characteristics of mesoscale fractures and applications to wide azimuth 3D P-wave seismic data. *Journal of Geophysics and Engineering*, *12*(3), p.448.

Wu, X., Chapman, M., Li, X.Y. and Boston, P., 2014. Quantitative gas saturation estimation by frequency-dependent amplitude-versus-offset analysis. *Geophysical Prospecting*, *62*(6), pp.1224-1237.

Xu, X. and Tsvankin, I., 2006. Anisotropic geometrical-spreading correction for wide-azimuth P-wave reflections. *Geophysics*, *71*(5), pp.D161-D170.